Mapping the Structure of the Corona Using Fourier Backprojection Tomography

Morgan, Huw; Habbal, Shadia Rifai; Lugaz, Noé

Published in:
Astrophysical Journal

DOI:
10.1088/0004-637X/690/2/1119

Publication date:
2009

Citation for published version (APA):
Morgan, H., Habbal, S. R., & Lugaz, N. (2009). Mapping the Structure of the Corona Using Fourier Backprojection Tomography. *Astrophysical Journal*, *690*(2), 1119-1129. https://doi.org/10.1088/0004-637X/690/2/1119

The Astrophysical Journal, 690:1119–1129, 2009 January 10 doi:10.1088/0004-637X/690/2/1119

MAPPING THE STRUCTURE OF THE CORONA USING FOURIER BACKPROJECTION TOMOGRAPHY

Huw Morgan[1,2], Shadia Rifai Habbal[1], and Noé Lugaz[1]
[1] Institute for Astronomy, University of Hawaii, 2680 Woodlawn Drive, Honolulu, HI 96822, USA; hmorgan@ifa.hawaii.edu
[2] Sefydliad Mathemateg a Ffiseg, Prifysgol Aberystwyth, Ceredigion SY23 3BZ, UK
Received 2008 June 30; accepted 2008 September 3; published 2008 December 2

ABSTRACT

Estimating the structure, or density distribution, of the solar corona from a set of two-dimensional white-light images made by coronagraphs is a critical challenge in coronal physics. This work describes new data-analysis procedures which are used to create global maps of the coronal structure at heights where the corona becomes approximately radial ($\geqslant 3\ R_{\odot}$). The technique, which is named Qualitative Solar Rotational Tomography (QSRT), uses total brightness white light observations, processed with a suitable background subtraction and a Normalizing Radial Graded Filter (NRGF). These observations are made with high frequency by the Large Angle and Spectrometric Coronagraph Experiment (LASCO) C2 coronagraph, which allows a standard Fourier-transform-based tomographical reconstruction. In this paper, we first test the technique using a model corona. QSRT is then applied to a set of observations made during Carrington Rotation (CR) 2000–2001 (2003 March 16 to 2003 March 31). Since the maps are constructed from data which are normalized using the NRGF process, QSRT cannot give electron density directly. Nevertheless, the tests using the model corona demonstrate the technique's ability to give a good qualitative reconstruction of the coronal structure at high latitude, with decreasing but acceptable accuracy at the equator. These tests also demonstrate QSRT's insensitivity to noise. For the LASCO C2 observations, good agreement is found between synthetic images calculated from the reconstructed corona and the original observations, and good agreement is found between the distribution of density in a QSRT reconstruction and that found using a global MHD model. Despite their lack of quantitative information on absolute electron density, the resulting maps (which are constructed directly from high-resolution coronal data observed at the appropriate height), contain useful information on the distribution of density in the corona.

Key words: solar wind – Sun: corona

Online-only material: color figures

1. INTRODUCTION

There is a large family of techniques aimed at estimating the three-dimensional distribution of density in the corona. Estimates of electron density are most commonly made from polarized brightness (*pB*) eclipse or coronagraph observations in the visible. Such observations are dominated by the Thomson-scattered disk emission by coronal electrons—the brightness is therefore proportional to the integrated electron density along a line of sight (LOS). The most basic technique is to assume a simple geometry for the corona (for example, spherical symmetry), and to invert the observed brightness directly (van de Hulst 1950; Saito et al. 1977; Quémerais & Lamy 2002). This robust technique is a reasonable approach when the corona possesses a simple geometry, for example, at the minimum of solar activity the assumption of a spherical or cylindrical symmetry is a good approximation, particularly over the poles. Refined estimates may be made by assuming more sophisticated geometries (Guhathakurta et al. 1996; Gibson et al. 2003).

Extrapolations of the observed photospheric magnetic field into the corona under certain boundary conditions can give an estimate of the position of the heliospheric current sheet (HCS). This technique is called potential field source surface (PFSS) extrapolation (Altschuler & Newkirk 1969; Schatten et al. 1969; Wang & Sheeley 1992). Although an estimate of the position of the HCS does not give a density structure directly, high-density streamers are expected to lie mostly along the neutral line of the HCS, therefore PFSS extrapolations are often used as a proxy for coronal density structures (Wang et al. 1997). This works best at solar minimum—the technique is not as suitable for times when rapid changes occur in the photospheric field (Wang et al. 2000). Saez et al. (2005) showed the existence of high-density streamers at solar minimum that were not associated with the main HCS. Using the estimated position of the HCS as a constraint on the distribution of structure, the density in the corona may be calculated from *pB* coronagraph observations, leading in particular to a refined estimate of the electron density of streamers (Thernisien & Howard 2006; Saez et al. 2007). Sophisticated global MHD models, using the observed photospheric magnetic field as a boundary, also give an estimate of the density as well as other properties of the corona (Mikic et al. 1996; Usmanov 1996; Linker et al. 1999; Roussev et al. 2003).

A series of images made of the corona over a solar rotation shows a steadily changing appearance. This variation can be exploited by assuming it is solely due to the rotation of the corona, and a three-dimensional reconstruction may be built. This approach is called Solar Rotational Tomography (SRT). Various SRT techniques have been developed, and a comprehensive summary of the different approaches is given by Frazin (2000). Some of these techniques are based on variations of the tomographical Algebraic Reconstruction Technique (ART; Davila 1994). To date, the most comprehensive body of SRT work is based on the robust, regularized, positive estimate (RRPE) devised by Frazin (2000). The success of RRPE has enabled reconstructions even during solar maximum (Butala et al. 2005), and the development of reconstructions including time dependence is discussed by Frazin et al. (2005). These techniques aim to find a distribution of electron density in a three-dimensional corona that best satisfies a set of coronagraphic *pB* observations

made over half a solar rotation (half a rotation since both east and west limbs are observed), subject to some reasonable assumptions such as the smoothness of the reconstruction.

The problems inherent to SRT are listed by Panasyuk (1999). In brief, they are:

1. The corona changes structure over timescales less than half a solar rotation (∼2 weeks).
2. The whole corona is not observed (large regions are hidden behind the occulting disk of the coronagraph, and behind the Sun itself).
3. The coronal brightness drops very sharply with distance from the Sun, which leads to instability in any reconstruction technique based directly on these observations.

In addition, *pB* observations made by the Large Angle Spectroscopic Coronagraph (LASCO) C2 and C3 coronagraphs (Brueckner et al. 1995) over the last 10 years are generally limited to one or two observations a day, therefore, current reconstructions based on *pB* observations have poor longitudinal resolution. Ground-based coronagraphs are also subject to intermittent temporal coverage. All these factors make the use of Fourier backprojection tomography (the technique most commonly used in medical applications) very unstable for coronal observations, with large and insurmountable errors in the reconstructions, particularly near to the equatorial plane.

This paper introduces a new SRT approach based on Fourier backprojection tomography of normalized LASCO C2 total brightness observations. Since the data are normalized prior to backprojection, the resulting maps give a qualitative rather than quantitative picture of coronal structure. We therefore name the technique Qualitative SRT (QSRT). The data processing steps are described in Section 2.1. The method for backprojection is described in Section 2.2. The results of applying QSRT to a model corona are shown in Section 3. The results of applying QSRT on observations are presented in Section 4, including a comparison of observed images with synthetic images created from the reconstructed densities. An extensive discussion of the interpretation of densities in QSRT maps is given in Section 5, followed by a list of potential applications, and a discussion of QSRT in the context of the Solar Terrestial Relations Observatory (STEREO) mission. Conclusions are given in Section 6.

2. THE QSRT METHOD

2.1. Data Processing

To create one reconstruction of the corona, observations made over a period slightly longer than half a solar rotation are needed (∼15 days). It is important to choose a time period with uninterrupted observing, that is, data gaps of longer than ∼8 hr should be avoided. Throughout this paper, we use a set of data collected from the end of CR 2000 and the first half of CR 2001 (2003 March 16 to 2003 March 31) as a working example. The LASCO C2 coronagraph typically makes ∼50 total brightness (B_t) observations (and one or two *pB* observations) a day. For our reconstructions, it is sufficient to use one in every four B_t observations (i.e., about one observation every 2 hr, or approximately 1° of solar rotation), giving a dataset of around 200 observations. We also obtain all *pB* observations made over the same time period by LASCO C2. The *pB* is used to create a background suitable for subtraction from the B_t images. Each *pB* observation consists of four files, containing the full sequence of polarizing angles. The data used in this work were collected using the typical LASCO C2 observing parameters—the "orange" filter (∼540–640 nm), with image sizes of 1024 × 1024 pixels for the B_t images and 512 × 512 for the *pB* images. The following steps describe the processing of the LASCO data.

2.1.1. Calibration and Rebinning

The data are calibrated with the standard LASCO procedures included in the Solar Software package, written for IDL. The calibration corrects for the flat-field response of the detector, radiometric sensitivity, stray light, geometric distortion, and vignetting. The *pB* sequences are combined into single images of polarized brightness. After calibration, the data are in physical units suitable for quantitative analysis. The images are shifted so that the Sun center is at the center of the image. The B_t images are then rebinned to 512 × 512 pixels.

2.1.2. Noise Filtering

A point filter is applied to the *pB* and the B_t images. In essence, this filter replaces any pixels that have a reading higher or lower than a few standard deviations from the local median, with a value halfway between the pixel value and the local median. The process is then iterated until a set number of iterations have passed, or there are no pixels with outlying values found. Coronal images have an intrinsic sharp drop of brightness with distance from the Sun, we use a temporary "flattened" image to identify the abnormal pixels (flattened using the Normalizing Radial Graded Filter (NRGF), to be described later in this section; also see Morgan et al. 2006). These pixels are then corrected in the original nonflattened images.

2.1.3. Background Subtraction

For each *pB* image, the B_t image made closest in time is identified. The *pB* images are then subtracted from the B_t images, giving a set of what we call unpolarized brightness (*upB*) images. In the context of LASCO observations, *upB* has been described previously by Llebaria et al. (1999). It has also been used by Morgan & Habbal (2007c) as a proxy for the F corona, and by Morgan et al. (2006) as a background subtraction suitable for image processing. The set of *upB* images covering ∼ half a solar rotation are then combined into an average *upB* image, or an ⟨*upB*⟩ image. ⟨*upB*⟩ images calculated for LASCO C2 are remarkably stable over the solar cycle at heights above ∼2.6 $R_\odot$ (Morgan & Habbal 2007c). The ⟨*upB*⟩ image is subtracted from the set of ∼200 B_t images. A calibrated image with background subtraction applied is shown in Figure 1(a). The validity of using ⟨*upB*⟩ as a suitable background for subtraction was discussed by Morgan et al. (2006). In brief, the combination of applying ⟨*upB*⟩ subtraction and NRGF processing to B_t observations leads to images which are almost identical to NRGF-processed *pB* observations.

2.1.4. NRGF Processing ("Flattening" the Image)

NRGF processing starts by calculating the mean and standard deviation of brightness, as a function of height, within the images. In previous work on image processing, we calculate these values for a single observation. For this work, we calculate single mean and standard deviation profiles (as functions of height) over the set of all ∼200 observations. These are plotted in Figure 2(a). The coronal brightness has a steep gradient with height. One may naïvely remove this gradient from an image by simply subtracting the mean brightness at each height. However,

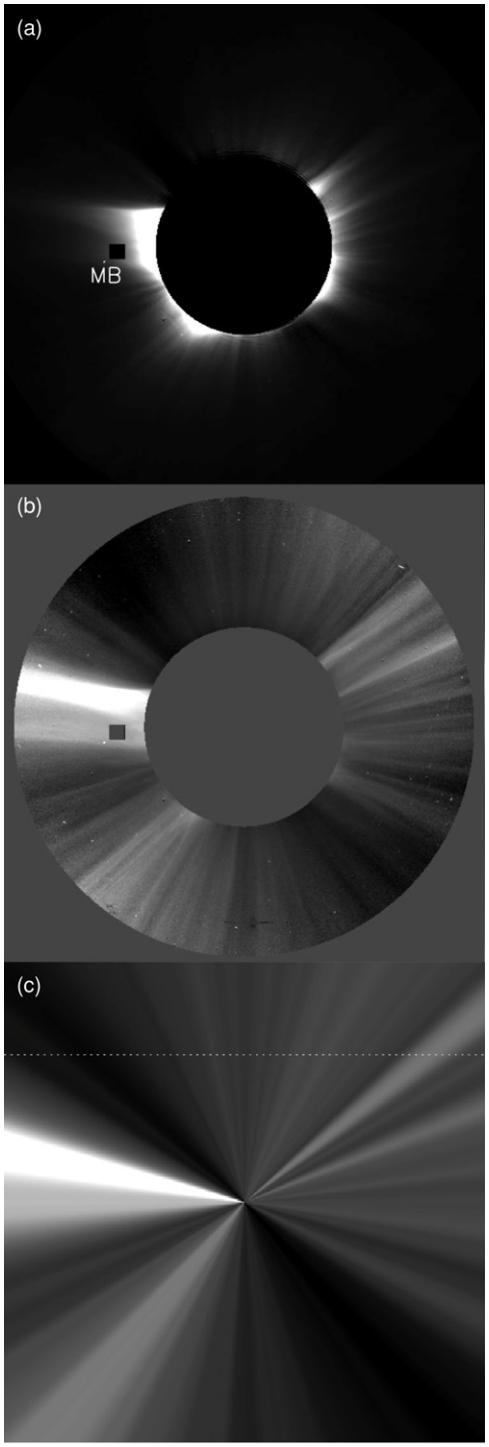

Figure 1. LASCO C2 image at different stages of processing. (a) Calibrated image taken at 2003 March 27 13:53 with background subtracted. A missing 16 × 16 pixel block has been labelled MB. (b) The same image processed with the NRGF (with heights from Sun center below 2.6 $R_\odot$ or above 6 $R_\odot$ set to an uniform arbitrary level). (c) Radial normalized brightness image, with all points interpolated from the latitudinal profile of Figure 2(b). This is the final image used for Fourier backprojection. The horizontal dotted line in (c) is of relevance to Section 2.2.

the contrast between bright and dark regions is large near the Sun, and very small far from the Sun. This information is contained in the standard deviation of brightness as a function of height. This is the dashed line in Figure 2(a). Figure 2(a) shows that the contrast between bright and dark regions is of the same order as the mean brightness at low heights, and actually drops faster than the mean brightness with height. An effective method of "flattening" a coronal image to reveal structure is to subtract the mean, then divide by the standard deviation. Therefore the normalized brightness $\tilde{B}$ of the NRGF-processed image is

$$\tilde{B} = [B_t - \langle B \rangle(\rho)] / \sigma(\rho), \quad (1)$$

where $\langle B \rangle$ and σ are the mean and standard deviations of brightness, respectively; ρ is the height measured from disk center. We apply NRGF processing to all images, and with this step, all quantitative radiometric information is lost. An NRGF processed image is shown in Figure 1(b).

2.1.5. Replacing Missing Blocks

LASCO images occasionally suffer from "missing blocks", where a rectangular area of the image has zero counts. These areas are too large to be filtered effectively by a point filter. A missing block is labelled "MB" in Figure 1(a). Latitudinal profiles from heights below and above any missing block regions are used to radially interpolate $\tilde{B}$ within the region. It is easier to accomplish such radial interpolation after the NRGF processing, since the image is so effectively flattened.

2.1.6. Creating a Radial Image

At heights above ∼3 $R_\odot$, the NRGF image shows a structure which is almost totally radial. This is illustrated in Figure 2(b), which shows, as a function of position angle (measured counter-clockwise from north), the range of normalized brightness gained from Figure 1(b) between heights of 3 and 5 $R_\odot$ (after point filtering and filling missing blocks). This range is very small, which shows that the corona must be very close to radial at these heights. The average profile of normalized brightness, as a function of position angle (averaged between 3 and 5 $R_\odot$), is used to create Figure 1(c). This is the final image used for backprojection. Each pixel in the image has a normalized brightness interpolated directly from the average profile shown in Figure 2(b) (the solid line). The normalized brightness is extended into the center and out to the extreme edges of the image. This is a strange-looking corona—the Sun has shrunk to a point, the corona is perfectly radial, and there is no drop in brightness with height. At any given height, the average brightness is zero, and the standard deviation of brightness is one. There are two main advantages of taking the average of the flattened image between 3 and 5 $R_\odot$ in comparison to only taking a single slice at one height. First, it helps to reduce noise and the influence of occasional errors in isolated pixels. Second, the influence of coronal mass ejections (CME) is reduced.

2.1.7. Final Rebinning

It is desirable in Fourier backprojection tomography for the image size perpendicular to the axis of rotation (the projections, or horizontal slices in the case of our coronal images) to contain approximately the same number of elements as the number of viewing angles. Therefore the images are rebinned (bilinear interpolation) to a managable ∼201 × 201 pixels and the whole data cube has ∼8 million elements (200 images of size 200 × 200 pixels). In principle, one could use all LASCO C2 B_t observations over half a rotation (∼800 images) and reconstruct using an image size of 800 × 800 pixels, although for the extra computational load, there is no great improvement in the results. For our current reconstructions, once the data are downloaded to

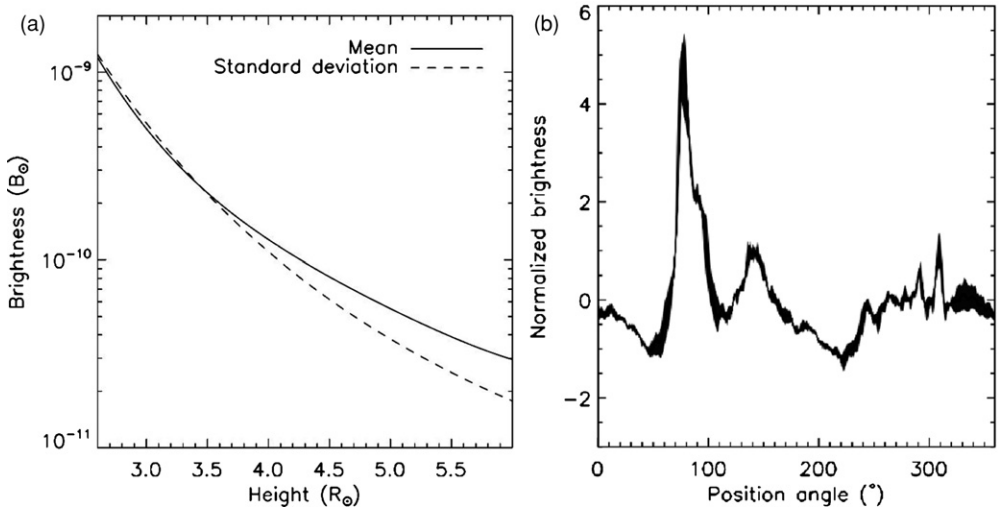

Figure 2. (a) Mean (solid line) and standard deviation (dashed line) of brightness as a function of height from Sun center calculated for the ∼200 observations made between 2003 March 16 to 2003 March 31. These are the profiles used by the NRGF process to "flatten" the image of Figure 1(a), resulting in Figure 1(b). (b) The solid line shows the average, and the shaded region the minimum–maximum range, of normalized brightness values measured in the flattened image of Figure 1(b) between heights of 3 and 5 $R_{\odot}$. The average profile is used to create the final radial brightness image of Figure 1(c).

the local machine (a PowerMac G5 with 2Gb memory), the data processing takes about 5 minutes, and the tomography itself less than a minute. The language used is IDL, and we have taken full advantage of IDL's array-manipulating abilities.

2.2. Fourier Backprojection

Fourier backprojection tomography, based on the Fourier slice theorem, is commonly used in medical and engineering applications. The implementation of Fourier backprojection on the processed LASCO C2 data is based directly on the formulations described in Chapter 3 of Kak & Slaney (2001; henceforth referred to as KS). Although Fourier backprojection is simple to implement on a computer (see Section 3.3 of KS), complications arise when the LASCO C2 observation geometry is considered rigorously. In particular, despite the large distance from the *Solar and Heliospheric Observatory* (*SOHO*) to the Sun, the LOSs of LASCO C2 through the corona are not exactly parallel (small detector, large corona) and the considerations for fan-shaped projections on an equally-spaced collinear detector described in Section 3.4.2 of KS become relevant. In addition, since the Sun's axis of rotation can be tilted towards or away from the observer (solar B_0 angle), we must apply the backprojection on the whole two-dimensional image (if the axis of rotation was not tilted, backprojection could be applied individually to horizontal image slices). We therefore follow the implementation for three-dimensional projections described in Section 3.6 of KS. With fan-shaped projections, to provide adequate 360° coverage of the three-dimensional reconstruction volume, data covering slightly more than half a solar rotation must be used, and appropriate filtering applied to a small set of the data observed outside the half-rotation period. This consideration is described in Section 3.5 of KS.

Figure 1(c) has a white dotted line plotted along the horizontal. If we define the observer's x and y axes as the image horizontal and vertical with the origin at the Sun's disk center (so that the y-axis points north), the white dotted line is at $y = 2.7\ R_{\odot}$. Figure 3(a) shows $\tilde{B}$ (the NRGF-processed brightness) plotted along this line. The appropriate transform of $\tilde{B}$ for backprojection is given by Equation (69) in Chapter 3 of KS. This is shown as the dashed line labelled "Q" in Figure 3(a). The transform is applied to all horizontal slices within the set of ∼200 images. A transform of the whole image of Figure 1(c) is shown in Figure 3(b). This is a Q image. The Q image must be backprojected onto our reconstruction surface. The reconstruction surface is a shell of points at a uniform height of 4 $R_{\odot}$, with a grid of 720 × 360 elements aligned regularly in 0.°5 increments of solar longitude and latitude. For each observation date (or equivalently, viewing angle), the position of each point in the reconstruction surface can be mapped onto the Q image plane, and values of Q are interpolated for each point from neighbouring points in the Q image. To illustrate this backprojection method, Figure 3(b) has a white ellipsoid which is actually a circle on the reconstruction surface, passing through the poles at latitudes 0° and 180°, and aligned along longitudes 90° (or 270°). For each observation date, a new Q image is produced, and this circle will map onto new coordinates in the image plane. So, for each point in the reconstruction surface, there are a set of ∼200 Q values obtained from the whole set of observations. Figure 3(c) shows the reconstruction surface obtained from a backprojection of the Q image of Figure 3(b). There are ∼200 such backprojections, one for each observation.

The backprojected Q values are weighted according to ρ^2/r^2, where r is the height of the point in the reconstruction surface (this is the same for all points), and ρ is the plane-of-sky height, or the height of the point projected onto the image plane. ρ of course varies according to viewing angle, or the longitude of the point relative to the Sun–observer line. The weighting is unity when $\rho = r$, or when the point is in the plane of sky ±90° relative to the Sun–observer line. The weighting is lowest when the point is at longitude 0° or 180° relative to the Sun–observer line (when ρ is at a minimum). This is illustrated in Figure 4 for a reconstruction point in the equatorial plane, and a point with a latitude of 45°. Of course, for a point in the equatorial plane, the weighting can reach zero. For latitudes further from the equatorial plane, the effect of the weighting is decreased. All viewpoints (or observing dates) are backprojected into the reconstruction surface and averaged according to the weighting ρ^2/r^2, giving a final reconstruction.

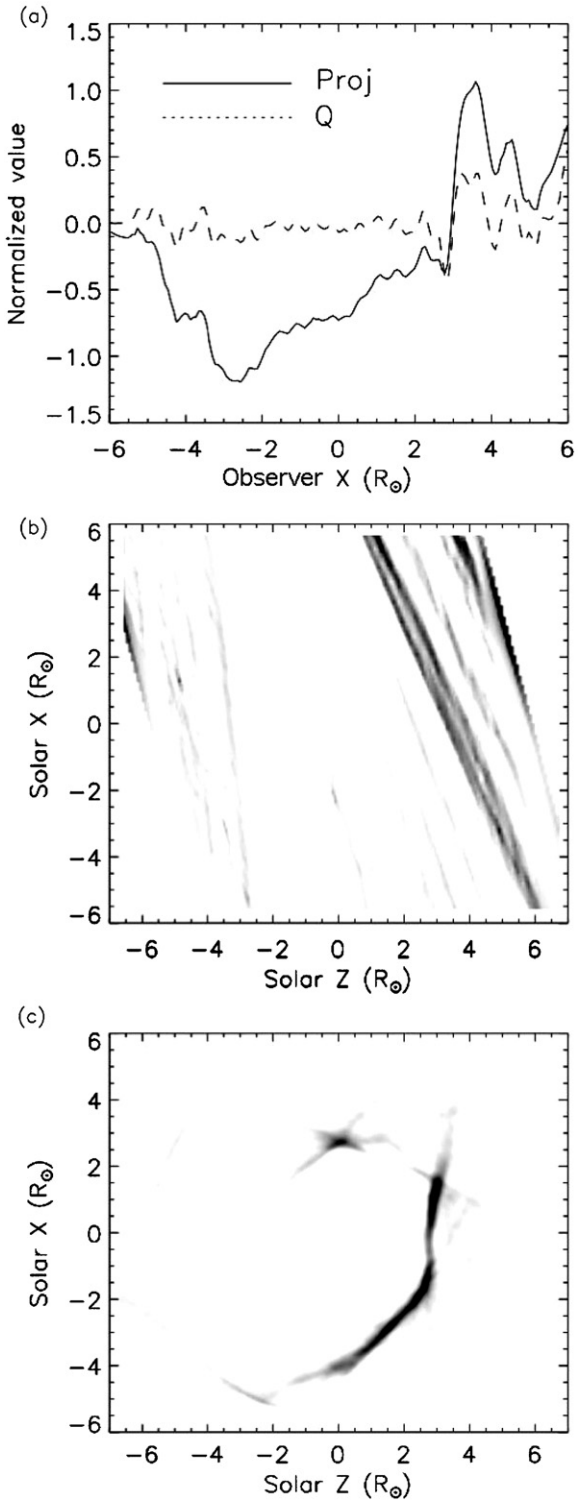

Figure 3. (a) Solid line is $\tilde{B}$ plotted along the white dotted line shown in Figure 1(c). The dashed line is Q, a transform of $\tilde{B}$ used for backprojection (see the text, or Equation 69 in Chapter 3 of KS). (b) The whole image of Figure 1(c) transformed according to Equation (69) in Chapter 3 of KS (a Q image). The white ellipsoid maps a circle of points in the reconstruction surface, mapped onto the image according to the appropriate viewing angle. (c) The backprojection of the Q image shown in (b) onto the reconstruction surface (with appropriate weighting, see the text).

As a final step, the reconstruction is thresholded so that negative values are all set to zero. This is found to improve the qualitative agreement of structure distribution between

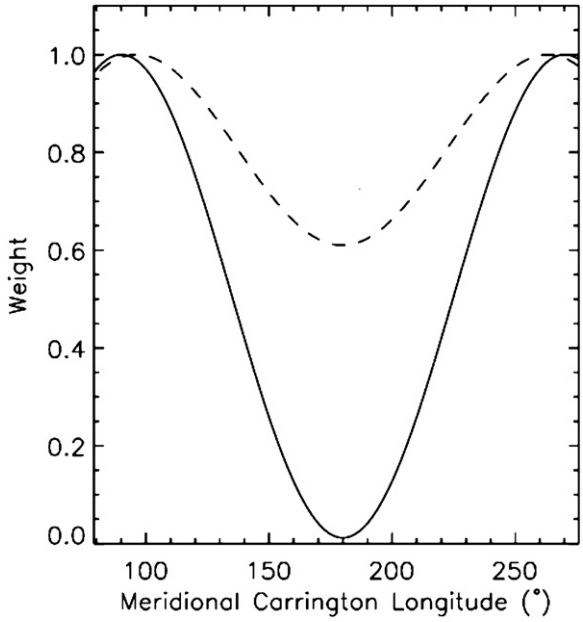

Figure 4. Weighting applied to the backprojection as a function of longitude (or the longitude of the point in the reconstruction surface relative to the Sun–observer line). The solid line is for a point in the equatorial plane (latitude 0°), and the dashed line is for a point with a latitude of 45°. For both cases, the weighting (ρ^2/r^2) is the highest when the point is in the plane of the sky relative to the observer (at ± 90° longitude relative to the Sun–observer line).

reconstructions and corona in tests involving a model corona and synthetic observations (see Section 3), and also improves the agreement between real observations and synthetic observations created from reconstructions.

3. QSRT APPLIED TO A MODEL CORONA

A model corona is created which is purely radial. In the model corona, a high-density band with varying width and latitude is placed near the equatorial plane, resembling the heliospheric current sheet near solar minimum. Smaller high-density structures are placed at mid-latitudes resembling isolated mid-latitude streamers. A longitude–latitude map of the coronal density at a height of 4 $R_\odot$ is shown in Figure 5(a). Similar to formulations given by Guhathakurta et al. (1996), the density within the model corona is given by

$$N_e(r,\theta,\phi) = N_p(r) + [N_s(r) - N_p(r)]\, f(\theta,\phi), \qquad (2)$$

where $f(\theta,\phi)$ is a function with values between 0 and 1 describing the distribution of density in longitude and latitude. $N_p(r)$ is the radial profile of electron density found within a coronal hole by Doyle et al. (1999), given (in cm^{-3}) by

$$N_p(r) = \frac{1.0\times10^8}{r^8} + \frac{2.5\times10^3}{r^4} + \frac{2.9\times10^5}{r^2}, \qquad (3)$$

with r in units of $R_\odot$. $N_s(r)$ is the radial profile of electron density found within an equatorial streamer's core by Gibson et al. (2003), given by

$$N_s(r) = \frac{3.6\times10^8}{r^{15.3}} + \frac{9.9\times10^7}{r^{7.34}} + \frac{3.65\times10^7}{r^{4.31}}, \qquad (4)$$

again with r in units of $R_\odot$.

The model corona is viewed from 200 different viewing angles between 0° and 180°. For each viewing angle, integrations

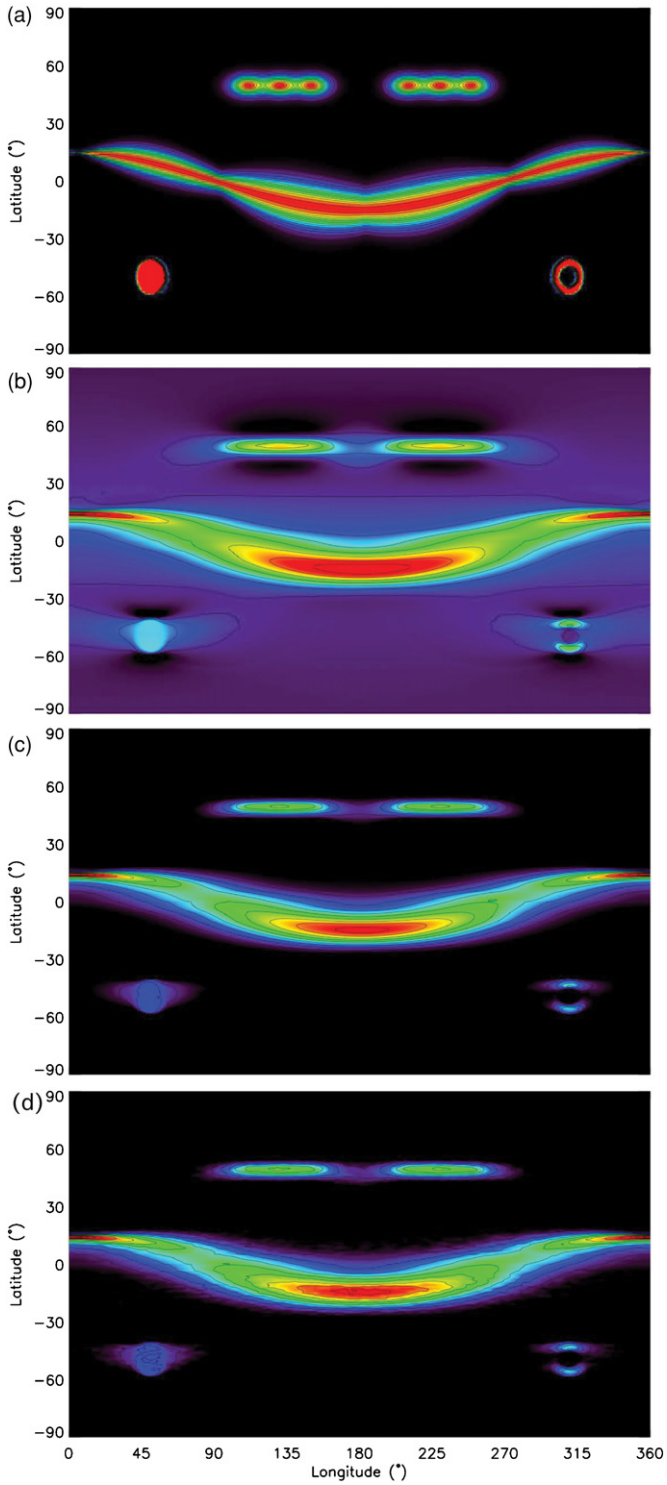

Figure 5. (a) Longitude–latitude map of electron density in a model corona at a height of 4 $R_\odot$, used to test the QSRT technique. Black is low density, and red is the highest. (b) QSRT reconstruction, also at a height of 4 $R_\odot$. (c) QSRT reconstruction with minimum-value thresholding (see text). (d) QSRT reconstruction with minimum-value thresholding, when 10% Gaussian noise has been added to the data.

(A color version of this figure is available in the online journal.)

along appropriate LOSs form a profile of polarized brightness as a function of position angle. Each LOS has a plane-of-sky (point of closest approach to the Sun) height of 4 $R_\odot$, and extends to each side of the plane of sky until the emission reaches 1% of

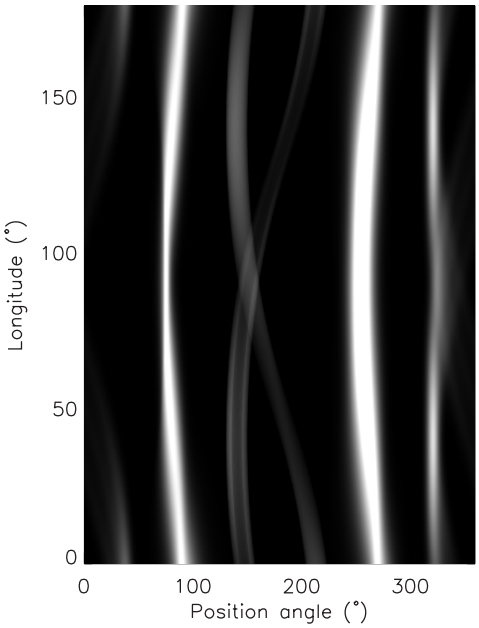

Figure 6. Brightness of the model corona at a height of 4 $R_\odot$ as a function of position angle and longitude (or viewing angle).

the plane-of-sky emission. We use 720 position angle bins, in increments of 0.°5 from 0 to 359.°5 (measured counter-clockwise from north). The observer is set in the equatorial plane, equivalent to observations of the corona with a B_0 angle of 0°. In contrast to a real observation, the LOSs are parallel. Figure 6 shows the brightness profiles obtained as a function of position angle and longitude (or viewing angle). The standard formulation for LOS integration for polarized brightness is given by, for example, Equation (1) of Quémerais & Lamy (2002).

This synthetic set of observations is normalized to a mean of zero and a standard deviation of one (as is described in Section 2.1), then used for the reconstruction methods described in Section 2.2. The result, for a reconstruction surface at a height of 4 $R_\odot$, is shown in Figure 5(b). In this map, all the basic high-density structure in the original corona is found, but the fine-scale detail such as the six distinct small "blobs" in the north mid-latitude (arranged in two rows of 3) is lost. High-density structures are also somewhat smeared in longitude. This is apparent in the south mid-latitude streamers. It should be stressed that the numbers contained in the reconstruction map do not give electron density. Since the observation is flattened, or normalized, this information is lost. What the technique gives us is a way of estimating the distribution of density structures. The reconstructed map has a mean of zero. Another artifact of flattening the coronal brightness prior to tomography is the appearance of low-density regions to the north and south of high-density structures in the reconstruction. An effective and simple way of removing these artifacts, and improving the agreement between reconstruction and the original corona is to threshold all values in the reconstruction to a minimum value. It is found that setting the minimum value at the mean value of the reconstruction gives optimum agreement. For these reconstructions created from normalized data, the mean is zero. Figure 5(c) shows the reconstructed corona with all values below zero set to zero. Figure 5(d) shows a reconstruction made from data with 10% Gaussian noise added to the observed coronal brightness. The reconstruction is still effective at revealing the position of high-density structure in the corona even with the added noise.

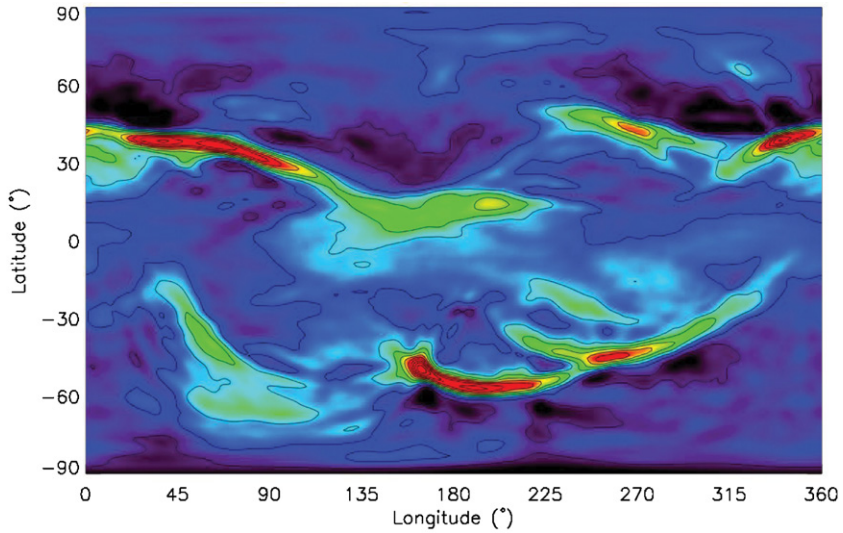

Figure 7. Longitude–latitude map of the coronal density distribution at a height of 4 $R_\odot$ determined using the QSRT technique for LASCO C2 data observed during the period 2003 March 16 to 2003 March 31. Red is high density, black is low. For clarity, a small smoothing window (of width 3° × 3°) has been applied.

4. QSRT APPLIED TO OBSERVATION

Figure 7 shows a longitude-latitude map of density at a height of 4 $R_\odot$, as gained from QSRT for observation dates 2003 March 16–2003 March 31. The coronal structure is dominated by high-density bands, narrow in latitude and elongated in longitude. The density varies considerably along these bands, and no band extends continuously through all longitudes (i.e., wrap all the way around the Sun). The bands in the north lie mostly in a narrow latitudinal region between 0 and 45°, with one small region at longitude 270° lying at a higher latitude of 50°. In the north lies one continuous band that extends from 315° longitude to 220° (wrapping around the 360°), therefore is extended around almost 3/4 of the Sun at a latitude close to 30°. In the south, the high-density structures are more intermittent in longitude, and lie further poleward than the structures in the north. One structure, centered near longitude 55° and latitude −40° has almost a north-south orientation, in contrast to all of the other high-density structures, which lie along more constant latitudes (i.e., with an east-west orientation). This structure seems to be associated with a large active region on the Sun.

4.1. Comparison of Real and Synthetic Observations

A nonrigorous test for the accuracy of the reconstruction can be made by creating synthetic observations and comparing to the original observations. We do this for many dates of observation over the half-solar rotation. Five such comparisons are shown in Figure 8. For each observation date and time, we create a synthetic image. For each pixel in the observed image, we calculate a set of coordinates corresponding to an appropriate LOS through the reconstructed corona (with height restricted to a maximum of 8 $R_\odot$). The "density" is interpolated within the reconstruction volume for points along the LOS, weighted according to ρ^2/r^2, then integrated along the LOS. This is then the image value at that pixel. Note that we do not use the standard formulation for LOS integration of coronal electron density (van de Hulst 1950; Quémerais & Lamy 2002). A similar approach is taken to build the synoptic maps of Figure 9. For the observed synoptic map we extract a latitudinal profile at 4 $R_\odot$ from all LASCO C2 observations in the data set. We then stack these profiles in time to create the displayed map. The procedure for creating the synthetic synoptic map is identical to the method for creating the synthetic images of Figure 8, with appropriate LOSs to create the latitudinal profiles.

As seen in Figures 8 and 9, good agreement is found between the true and synthetic images, even down to surprisingly fine spatial scales. Since this agreement is found over the half-solar rotation, we can have confidence in the accuracy of the density distribution shown in Figure 7. The structures seen in the images of Figure 8 or in the profiles of Figure 9 can be quickly compared to the three-dimensional structures seen in the density map of Figure 7 by adding 90° to the meridional longitude for the west limb, and subtracting 90° for the east limb (and wrapping around 360°). For example, for the top image of Figure 8, observed with meridional Carrington longitude 20°, the structure which gives rise to the appearance of the corona on the west limb can be viewed in the density map at longitude 110° (20°+ 90°), and the east limb structure at longitude 290° (20–90°, wrapped around 360°). In the synoptic maps of Figure 9, the east limb is at position angle 0–180° and the west is 180–360°.

Despite the general success of QSRT, there are some significant discrepancies between the real and synthetic observations shown in Figures 8 and 9. The relative brightness of structures is often inaccurate, and some low-brightness structures are missing, or, conversely, we have false detections of low-brightness structures. These inaccuracies are likely due to the loss of quantitative information when the NRGF flattening process is applied—a necessary prerequisite of the QSRT technique. As shown in Section 3, the reconstructed corona shows the accurate position of high-density structures, but does not accurately potray the relative density of structures. True observations are also subject to correlated errors or uncertainties such as gradual or rapid temporal changes, with the density of some structures changing in time, or even appearing or disappearing. Related to this is the "contamination" of observations by transient events. We do not usually remove observations which contain small CMEs, and such events must be detrimental to the accuracy of the reconstruction. CMEs may also lead to a sudden long-term change in the distribution of structure. See, for example, a bright CME in the observed synoptic map of Figure 9, at decimal Carrington longitude 2001.4 and position angle

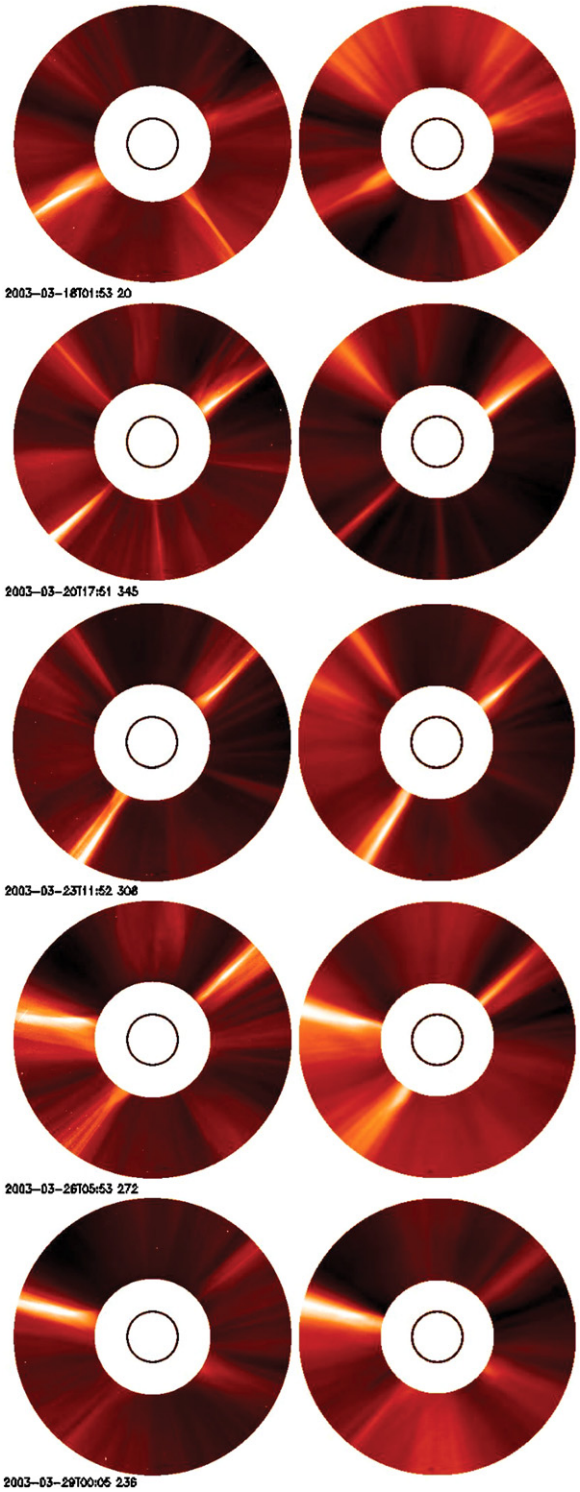

Figure 8. Comparison of observations (left column) with synthetic observations created from the QSRT reconstruction (right column). The five observation-model pairs are for different dates, from top to bottom: 2003 March 18, 2003 March 20, 2003 March 23, 2003 March 26, and 2003 March 29. These dates correspond to solar rotation increments of ∼36°, from top to bottom the meridional Carrington longitudes are: 20, 345, 308, 272, and 236°. The inner ring in all images shows the position of the Sun. The field of view is 2.6–6 $R_\odot$. All images are processed with the NRGF.

(A color version of this figure is available in the online journal.)

250°. Such sudden events cannot be reconstructed using QSRT, and the brighter the event is, the greater the disruption to the reconstruction.

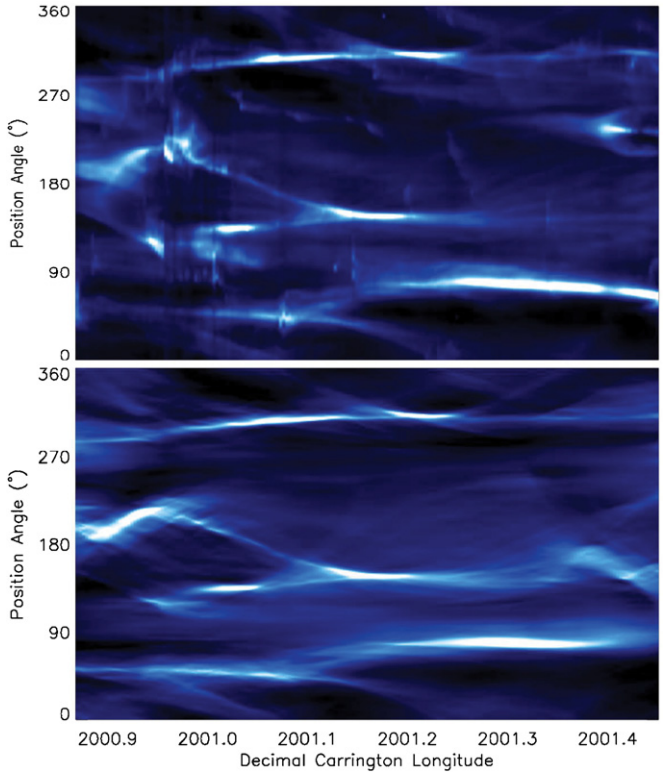

Figure 9. Synoptic maps of the corona for the whole observational period. The maps are constructed from latitudinal profiles at a height of 4 $R_\odot$, stacked in time from left to right. The vertical axis is position angle, or angle counterclockwise from north. The horizontal axis shows decimal Carrington Longitude at the meridian. The top plot is the observed synoptic map, the bottom is a synthetic map created from the QSRT reconstruction.

(A color version of this figure is available in the online journal.)

4.2. Comparison with PFSS and Global MHD Results

The top plot of Figure 10 shows again the QSRT longitude–latitude map at 4 $R_\odot$, with a dashed white line showing the position of the HCS, or neutral line, estimated by PFSS extrapolation of photospheric magnetic field observations made over CR 2001 by the Wilcox Solar Observatory (WSO)[3]. For this plot, we have shown the PFSS extrapolation with the source surface at 3.25 $R_\odot$. This is the PFSS extrapolation with the best correlation between the distribution of structure in the QSRT map and the position of the HCS. The QSRT map shows intermittent distribution of structure along the HCS, but has also found many high-density structures not associated with the HCS. This supports the finding of Saez et al. (2005), who concluded that not all high-density streamers lie along the main HCS, even close to solar minimum.

The bottom plot of Figure 10 shows density at a height of 4 $R_\odot$ as calculated using a large-scale global MHD (GMHD) model, based on magnetic field observations of the photospere over a solar rotation centered on date 2003 March 23 (which is the central date of the QSRT reconstruction). The GMHD map contains far more structural information than the HCS estimate of PFSS. The reasonable correlation between structures in the GMHD and QSRT map is satisfying, since the two results are obtained independently from very different types of observations, and using very different approaches. Immediately one

[3] See http://wso.stanford.edu for details of the photospheric observations and the PFSS extrapolations.

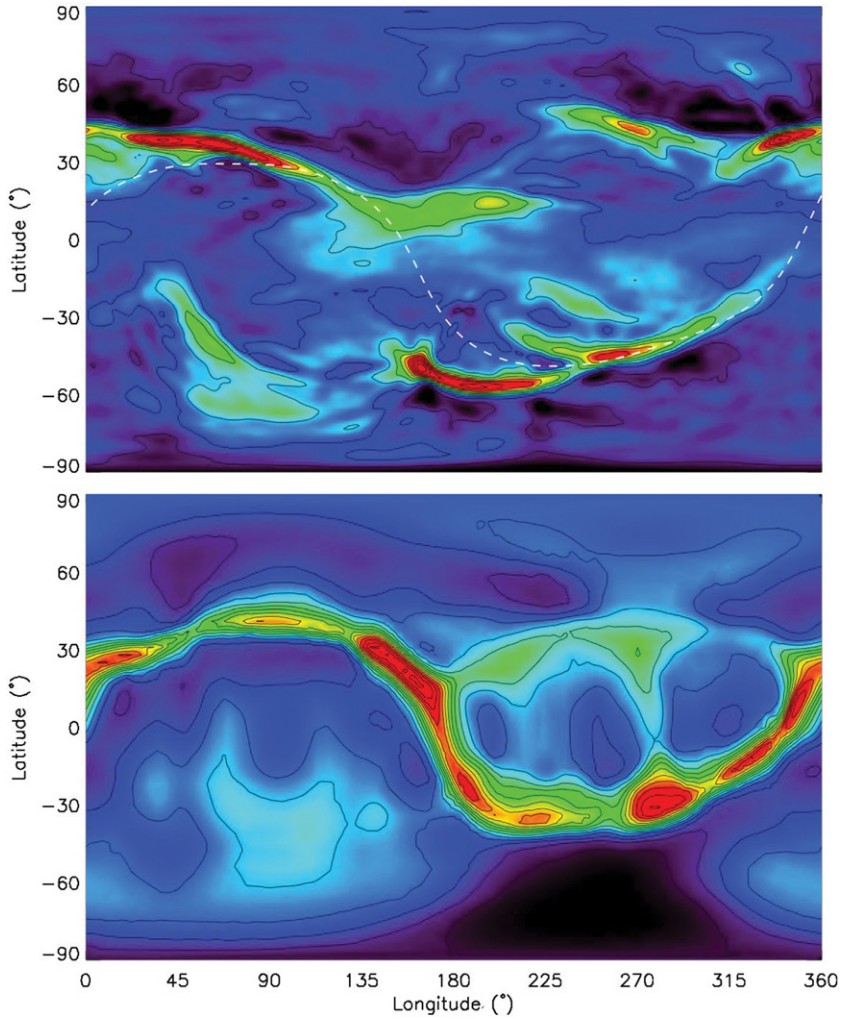

Figure 10. Top: QSRT map with white dashed line showing the position of the HCS calculated using a PFSS extrapolation of photospheric magnetic field observations. Bottom: density at a height of 4 $R_{\odot}$ calculated using a global MHD model.

can see the usefulness of the QSRT maps in validating the results of models, despite containing only qualitative information on density. The QSRT map is constructed directly from coronal observations, and needs only half a solar rotation of data for the reconstruction, whereas the GMHD and PFSS methods need a whole rotation of photospheric observations. For this reason, QSRT can achieve better temporal resolution than models based on photospheric field observations. Due to issues of computational efficiency and the processing of photospheric field data, the QSRT method can currently achieve far better spatial resolution than GMHD. QSRT is also based directly on observations of the corona, and is therefore less dependent on assumptions than GMHD. However, QSRT lacks the quantitative information on density (and other physical parameters such as magnetic field) given by GMHD. The two approaches are complimentary, and this will be explored further in a subsequent study.

5. DISCUSSION

5.1. Interpretation of QSRT Results

If one had perfectly clean observations of an unchanging corona over half a solar rotation (and somehow observe the whole corona including the region hidden behind the Sun), one could apply Fourier backprojection tomography and regain a map of the true electron density structure. In practice, of course, no observation is without error, and the corona changes—even at the minimum of activity there will be some change in density, and therefore brightness. As seen in Figure 1(b), there is a ∼2 order of magnitude drop in brightness in the corona between the inner and outer field of view of LASCO C2 (2.3–6 $R_{\odot}$). Therefore a 1% measurement error in brightness at small heights is about equal to the observed brightness at large heights. Roughly speaking, a backprojection of the brightness at small heights containing the 1% error would make the whole reconstruction process at large heights unfeasible. The same arguments would apply to a small variation in brightness with time. Even a very minor variation at low heights would destroy the backprojection process at large heights. To make any headway with real observations, the brightness gradient must be removed prior to backprojection. In fact, both the steep gradient in mean brightness and standard deviation of brightness must be removed, and this is the justification for applying NRGF processing.

How can the reconstruction density map created from flattened coronal data (NRGF-processed) be interpreted? The reconstruction "densities" have a mean close to zero at all heights, and the densities cannot be transformed easily into electron density. As shown in Figures 8 and 9, when the reconstruction volume is integrated to create synthetic observations, we regain the original NRGF-processed observations

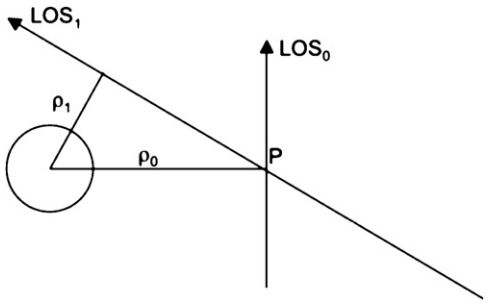

Figure 11. Simple geometry of two LOSs (LOS_0 and LOS_1) passing through a point P in the corona. The circle is the Sun, and ρ_0 and ρ_1 are the perpendicular distances from the LOS to the Sun center (or distance of the point of closest approach).

very closely. We are confident therefore that the density maps contain accurate information on the distribution, or position, of structures in the corona. It is the quantities that are difficult to interpret, and this is the most troubling aspect of QSRT.

The NRGF processing prior to backprojection is equivalent to an additional weighting, or filtering, on the backprojection. This argument is presented with the aid of Figure 11. Consider a point P in the reconstruction volume. If backprojection was applied to the original, unflattened images (that is, with a steep gradient of brightness with height), LOS_1 would have a far greater influence on P than would LOS_0—the brightness for LOS_1 would be greater than for LOS_0 since $\rho_1 < \rho_0$. However, NRGF processing filters the original brightness according to the mean and standard deviation of brightness, which are steep functions of ρ, the distance of an image pixel from Sun center. The original brightness for LOS_1 has a large mean brightness subtracted, and is divided by a large standard deviation of brightness (see Figure 1(b) and Equation 1). In comparison to backprojection using nonflattened brightness, QSRT allows LOS_0 a far greater influence on P compared to LOS_1.

The NRGF filtering is essential to enable backprojection tomography to work on coronal data. However, the filtering also results in a reconstruction density which is far removed from the true electron density, and there is no straightforward step to transform the QSRT reconstructions into absolute electron densities. Despite this limitation, we have gained a high-resolution map which shows an accurate distribution of structure, even though the relative strength of peaks within the map may be inaccurate. Certainly these maps could be used as a basis for calculating absolute electron densities. An ART-type or least-squares fitting algorithm scheme is envisaged where the position of structure is constrained directly by the results of QSRT, with the numerical values within the map adjusted until we gain true electron densities. For this, we would necessarily use the set of *pB* observations made over the appropriate time period as the fitting constraint. This approach will be presented in a future work.

5.2. Applications for QSRT

QSRT maps will prove most useful for the following applications.

- *Constraining models.* QSRT maps can be used to validate and possibly improve the results of large-scale coronal models, at least in predicting the distribution of density structures.
- *Interpreting other observations.* Knowing the three-dimensional structure of the corona will prove extremely useful in interpreting other types of coronal and heliospheric observations. The authors are already applying QSRT results in improving the diagnostic capabilities of Ultraviolet Coronagraph Spectrometer (UVCS)/*SOHO* observations. QSRT maps are also proving invaluable in modeling Interplanetary Scintillation (IPS) observations, resulting in improved constraints on solar wind velocity in the heliosphere reference.
- *Links between the Sun and corona.* Morgan & Habbal (2007a, 2007b) established links between observed structures in coronagraph observations (streamers) with structures viewed in extreme UV in the chromosphere and low corona. QSRT maps will give a much-improved constraint on the shape and position of structures in the corona, and enable a better interpretation of the coronal evolution from the Sun into the heliosphere.
- *Temporal evolution of coronal structure.* QSRT maps are reasonably quick to produce, and need half a solar rotation of uninterrupted observations to produce one xs reconstruction. A half-solar-rotation (∼14 days) sliding window through a large set of observations will provide a smoothed picture of large-scale changes in the corona over the solar cycle.

5.3. QSRT and STEREO

QSRT has immediate relevance to the two coronagraph instruments aboard the *Solar Terrestrial Relations Observatory* (*STEREO*) mission (Kaiser 2005; Matthews & Culhane 2007). These are the COR 1 and 2 coronagraphs, part of the Sun Earth Connection Coronal and Heliospheric Investigation's (SECCHI) package (Howard et al. 2002). There are two main benefits in comparison to using LASCO C2. Firstly, the COR 1 instrument observes down to very low heights in the corona, and maps of the density structure at these heights would enable a direct comparison with structures near the Sun (filaments, active regions, coronal holes). Secondly, since there are two spacecraft (*STEREO A* and *B*) looking at the corona from two different (longitudinal) viewing angles, QSRT reconstructions can be made in less than the ∼14 days necessary with only one viewpoint. For example, if the two spacecraft are separated by 90°, a reconstruction can be made with ∼7 days of observation. For a short period, when *STEREO A*, LASCO C2, and *STEREO B* are separated by 60° (or 120°) from each other, a reconstruction may be made with less than 5 days of observation.

6. CONCLUSIONS

QSRT is a new technique for estimating the distribution of structure in the solar corona. The technique's strengths are as follows.

1. *Robustness*, or tolerance of noise and temporal variations. For example, maps can be created for times of high solar activity when there are frequent CMEs. This makes QSRT a good technique for mapping the solar maximum corona, which can be problematic using other SRT techniques.
2. *High spatial resolution*. Due to its use of B_t observations which are made far more frequently than *pB* with LASCO C2, QSRT maps have high spatial resolution, and relatively fine-scale structure can be reconstructed.

3. *Computational efficiency*. Computer implementation of Fourier backprojection is quick and involves no iteration.
4. *Accuracy*. QSRT accurately estimates the distribution of most high-density structure, as shown by the comparison between observations and synthetic observations calculated from the reconstruction densities.

Nevertheless, QSRT does have some major limitations.

1. It results in qualitative maps. It does not give absolute electron density. Neither is there a simple transform to change the QSRT density into electron density.
2. Related to the previous point, the relative densities of structure within a map are likely inaccurate.
3. As with all SRT techniques, QSRT cannot show rapid temporal changes. Any temporal changes in the corona lead to inaccuracies in the reconstruction, although the use of NRGF filtering on the images prior to backprojection help reduce this detrimental effect.

Advances in observation and analysis tools will lead in the next years to systematic mapping of the global coronal density. We anticipate that such maps will be formed using a variety of complimentary observations and analysis techniques (based on coronagraphic, photospheric magnetic field, interplanetary radio, and in situ observations). As part of this goal, an atlas of QSRT maps constructed over the solar cycle observed to date by LASCO C2 will be published soon.

The author extends his gratitude to Malcolm Slaney for prompt correspondence. This work is supported by NASA grants NNX07AH90G and NNX07AK22G to the Institute for Astronomy. The *SOHO*/LASCO data used here are produced by a consortium of the Naval Research Laboratory (USA), Max-Planck-Institut Use fuer Aeronomie (Germany), Laboratoire d'Astronomie (France), and the University of Birmingham (UK). *SOHO* is a project of international cooperation between ESA and NASA. The Wilcox Solar Observatory's photospheric field data and extrapolations were obtained from the WSO section of Stanford University's Web site courtesy of J. T. Hoeksema. WSO is supported by NASA, the NSF, and ONR.

REFERENCES

Altschuler, M. D., & Newkirk, G. Jr. 1969, Sol. Phys., 9, 131
Brueckner, G. E., et al. 1995, Sol. Phys., 162, 357
Butala, M. D., Frazin, R. A., & Kamalabadi, F. 2005, J. Geophys. Res. (Space Phys.), 110, 9
Davila, J. M. 1994, ApJ, 423, 871
Doyle, J. G., Teriaca, L., & Banerjee, D. 1999, A&A, 349, 956
Frazin, R. A. 2000, ApJ, 530, 1026
Frazin, R. A., Butala, M. D., Kemball, A., & Kamalabadi, F. 2005, ApJ, 635, L197
Gibson, S. E., Foster, D. J., Guhathakurta, M., Holzer, T., & St. Cyr, O. C. 2003, J. Geophys. Res. (Space Phys.), 108, 7
Guhathakurta, M., Holzer, T. E., & MacQueen, R. M. 1996, ApJ, 458, 817
Howard, R. A., Moses, J. D., Socker, D. G., Dere, K. P., & Cook, J. W. 2002, Adv. Space Res., 29, 2017
Kaiser, M. L. 2005, Adv. Space Res., 36, 1483
Kak, A. C., & Slaney, M. 2001, Classics in Applied Maths 33, Principles of Computerized Tomographic Imaging (Philadelphia, PA: SIAM)
Linker, J. A., et al. 1999, J. Geophys. Res., 104, 9809
Llebaria, A., Lamy, P., & Koutchmy, S. 1999, in ESA Special Publication 446, 8th *SOHO* Workshop: Plasma Dynamics and Diagnostics in the Solar Transition Region and Corona, ed. J.-C. Vial & B. Kaldeich-Schü, 441
Matthews, S. A., & Culhane, J. L. 2007, Adv. Space Res., 39, 1791
Mikic, Z., Linker, J. A., & Colborn, J. A. 1996, BAAS, 28, 868
Morgan, H., & Habbal, S. R. 2007a, A&A, 464, 357
Morgan, H., & Habbal, S. R. 2007b, A&A, 465, L47
Morgan, H., & Habbal, S. R. 2007c, A&A, 471, L47
Morgan, H., Habbal, S. R., & Woo, R. 2006, Sol. Phys., 236, 263
Panasyuk, A. V. 1999, J. Geophys. Res., 104, 9721
Quémerais, E., & Lamy, P. 2002, A&A, 393, 295
Roussev, I. I., et al. 2003, ApJ, 595, L57
Saez, F., Llebaria, A., Lamy, P., & Vibert, D. 2007, A&A, 473, 265
Saez, F., Zhukov, A. N., Lamy, P., & Llebaria, A. 2005, A&A, 442, 351
Saito, K., Poland, A. I., & Munro, R. H. 1977, Sol. Phys., 55, 121
Schatten, K. H., Wilcox, J. M., & Ness, N. F. 1969, Sol. Phys., 6, 442
Thernisien, A. F., & Howard, R. A. 2006, ApJ, 642, 523
Usmanov, A. V. 1996, in AIP Conf. Ser. 382, ed. D. Winterhalter, J. T. Gosling, S. R. Habbal, W. S. Kurth, & M. Neugebauer (San Francisco, CA: AIP), 141–144
van de Hulst, H. C. 1950, Bull. Astron. Inst. Netherlands, 11, 135
Wang, Y.-M., & Sheeley, N. R., Jr. 1992, ApJ, 392, 310
Wang, Y.-M., Sheeley, N. R. Jr., & Rich, N. B. 2000, Geophys. Res. Lett., 27, 149
Wang, Y.-M., et al. 1997, ApJ, 485, 875